LANGMUIR

pubs.acs.org/Langmuir Article

# A Linear-Regression-Based Method for Determining Surface Tension from Variation in Interfacial Curvature

Carrie E. Perlman,* Bret A. Brandner, and Stephen B. Hall

Cite This: *Langmuir* 2025, 41, 23096−23108 Read Online

ACCESS | Metrics & More | Article Recommendations

**ABSTRACT:** We develop a new linear-regression-based method for determining surface tension, $\gamma$, from interfacial curvature. Across a static fluid−fluid interface, $\gamma$ is balanced by the difference in hydrostatic pressure, $\Delta P$. The balance is described by the Young−Laplace relation: $\Delta P = \gamma\,(k1 + k2)$, where $k1 + k2$ is the sum of the principal interfacial curvatures. Along the interface, $\Delta P$ varies linearly with elevation. It has been assumed that, even when there is surfactant at the interface, $\gamma$ is constant along the interface. If this assumption is correct, then, according to the Young−Laplace relation, $k1 + k2$ must also vary linearly with elevation. For images of a constrained sessile droplet and a captive bubble, each with an interfacial dipalmitoyl phosphatidylcholine (DPPC) monolayer that is compressed to varying degrees, we determine the offset in $\Delta P$ from that at a reference elevation, $\Delta P - \Delta P_o$, and $k1 + k2$ at interfacial points of different elevations. We find that $k1 + k2$ indeed varies linearly with elevation. Thus, if we plot $\Delta P - \Delta P_o$ versus $k1 + k2$, we obtain a linear plot with a slope equal to $\gamma$. We develop and make available an algorithm for determining $\gamma$ by linear regression. And we assess accuracy by comparison to $\gamma$ values determined by axisymmetric drop shape analysis. For a droplet or bubble with a DPPC monolayer, over a $\gamma$ range of 2−70 mN/m, the absolute value of the difference in $\gamma$ determined by the alternative methods averages 0.30 ± 0.37 mN/m. Further, while we apply the method to axisymmetric interfaces and make use of axisymmetry to determine the curvature from two-dimensional images, the underlying theory does not require axisymmetry. With 3D volumetric imaging, the method could potentially be extended to more complex interfacial geometries.

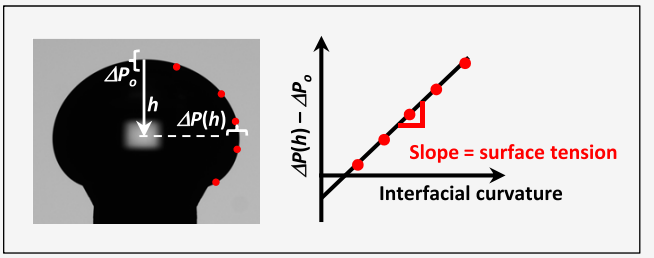


## INTRODUCTION

Across static fluid−fluid interfaces, the trans-interfacial hydrostatic pressure difference, $\Delta P$, balances surface tension, $\gamma$. The balance is described by the Young−Laplace relation:[1] $\Delta P = \gamma\,(k1 + k2)$, where $k1$ and $k2$ are the principal interfacial curvatures and we refer to $k1 + k2$ as the summed curvature. In the absence of or with negligible gravity (Bond number $Bo = \Delta\rho g L^2/\gamma \ll 1$, where $\Delta\rho$ is the difference between the densities of the fluids at the interface, $g$ is the gravitational constant, and $L$ is a characteristic length), interfacial curvature would be spherical. However, gravity morphs the interface from spherical. As such, curvature varies along the interface with elevation and, for $Bo > 1$, $\gamma$ can be determined from analysis of that variation in curvature.

Along an interface, gravity causes $\Delta P$ to vary linearly with elevation. Thus, according to the Young−Laplace relation, the summed curvature, too, would need to vary linearly with elevation in order for $\gamma$ to be constant along the interface. From the contour alone, $\Delta P$ cannot be determined. However, the offset in $\Delta P$ from $\Delta P$ at a reference elevation, $\Delta P - \Delta P_o$, can be calculated and also varies linearly with elevation. Thus, plotting $\Delta P - \Delta P_o$ versus the summed curvature should be informative. A nonlinear relation would indicate that the summed curvature varied nonlinearly with elevation and $\gamma$ varied along the interface. A linear relation would indicate that the summed curvature varied linearly with elevation and $\gamma$ was constant along the interface. Further, with a linear relation, the value of the slope would be the surface tension.

Surface tension determination from interfacial contour has been performed previously, and is performed in the present study, for axisymmetric interfaces. Existing methods assume $\gamma$ to be constant along the interface. An approach developed by Malcolm and Elliott employs numerical solution of the differential equation for the meridian curve of a droplet or bubble.[2] For this method, gravity-induced deviation from a spherical contour is specified by a shape factor that is a function of capillary length, $L_C = \sqrt{\gamma/(\Delta\rho g)}$, and $\gamma$ is assumed to be constant. An alternative approach, axisymmetric drop shape analysis (ADSA), employs differential equations parameterized as a function of an arc length variable along the

Received: June 3, 2025
Revised: July 25, 2025
Accepted: July 28, 2025
Published: August 20, 2025

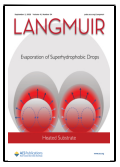





https://doi.org/10.1021/acs.langmuir.5c02838
*Langmuir* 2025, 41, 23096−23108

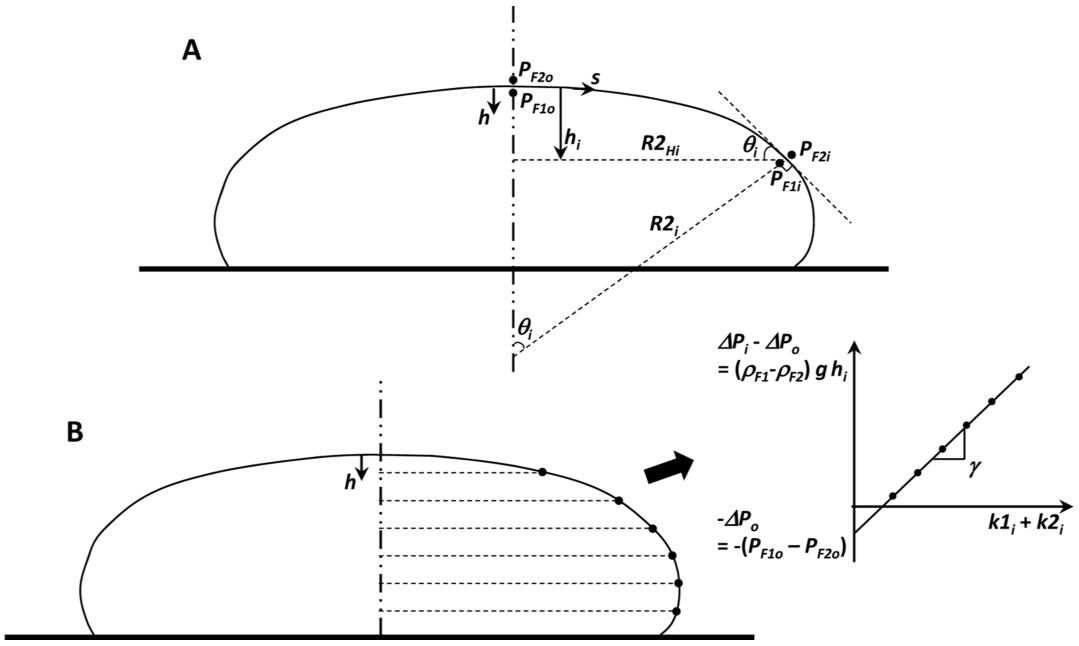


**Figure 1.** Regression-based surface tension determination method for a sessile droplet. (A) Schematic of sessile droplet. Depth below origin, *o*, at the top of the droplet indicated by *h*. Arc length variable *s* increases in clockwise direction along the interface on the right side of the droplet. Interfacial pressure drop $\Delta P$ is the difference between pressures $P_{F1}$ and $P_{F2}$ of fluids #1 and #2 inside and outside of the droplet, respectively. Pressures $P_{F1}$ and $P_{F2}$ vary hydrostatically, proportional to fluid densities $\rho_{F1}$ and $\rho_{F2}$, respectively. At depth $h_i$, interfacial tangent forms angle $\theta_i$ with horizontal, distance to central axis in direction normal to tangent is $R2_i$, and horizontal radius is $R2_{Hi}$. The angle between $R2_i$ and central axis is also $\theta_i$. (B) At multiple depths, one can determine (i) offset in $\Delta P$ from that at a reference elevation, $\Delta P_i - \Delta P_o = (\rho_{F1} - \rho_{F2})gh_i$, where *g* is the gravitational constant; and (ii) summed curvature $k1_i + k2_i$, where $k1_i$ and $k2_i = 1/R2_i$ are the principal interfacial curvatures that are determined as detailed in the text and Figure 3. Plotting $\Delta P_i - \Delta P_o$ vs $k1_i + k2_i$ yields a relation with an intercept equal to $-\Delta P_o = -(P_{F1o} - P_{F2o})$ and a slope equal to surface tension, $\gamma$. If the relation is linear, then $\gamma$ is constant along the interface.

interface.[1,3] The solution of the equations comprises numerical integration, optimal fitting of a theoretical curve to an experimentally-captured interfacial contour, and an assumption that $\gamma$ is constant.

ADSA typically yields an excellent fitting of the theoretical curve to the experimental interfacial contour, which suggests that the assumption of constant $\gamma$ is appropriate. However, for droplets or bubbles with surfactant monolayers, whether the summed curvature varies linearly with elevation and $\gamma$ is constant along the interface has not, to our knowledge, been directly explored. And it is not a given that $\gamma$ be constant. Along a static interface with a surfactant monolayer, Marangoni forces tend to normalize the surfactant concentration and thus $\gamma$. However, interfacial surfactant concentration, and $\gamma$, can vary when Marangoni forces are opposed by other forces. In a soap bubble, for example, Marangoni forces are balanced by fluid weight. Over the height of a large soap bubble, $\gamma$ can vary ~100%.[1]

Here, for the particular systems of a droplet and a bubble with dipalmitoyl phosphatidylcholine (DPPC) monolayers, we test the assumption that $\gamma$ is constant. We evaluate the variation in summed curvature with respect to elevation, thus performing our analysis in the direction of action of the gravitational force that deforms the interface from spherical.

## METHODS

We first present relevant theory and develop an algorithm for using linear regression to determine $\gamma$. We next detail experimental methods for imaging and analyzing sessile droplets and captive bubbles with or without interfacial monolayers compressed to different surface tensions. We finally detail metrics for validating regression-determined surface tension, $\gamma_{\text{Regression}}$, by comparison to ADSA-determined surface tension, $\gamma_{\text{ADSA}}$ (software purchased from Neumann, W. A., University of Toronto).

**Theory.** Consider a sessile fluid droplet (Figure 1A). Across the interface at the origin, at the top of the droplet where depth $h \equiv 0$, there is pressure difference $\Delta P_o = P_{F1o} - P_{F2o}$, where $P_{F1}$ and $P_{F2}$ are the pressures in fluids 1 and 2, respectively. At a greater depth, $h_i$, $\Delta P_i = P_{F1i} - P_{F2i}$. The pressures at the two depths are related by hydrostatic variation

$$P_{F1i} - P_{F2i} = (P_{F1o} + \rho_{F1}gh_i) - (P_{F2o} + \rho_{F2}gh_i) \quad (1)$$

where $\rho_{F1}$ and $\rho_{F2}$ are the densities of fluids 1 and 2, respectively. Note, $P_{F1o}$ and $P_{F2o}$ are not known, though their difference, $\Delta P_o$, can be determined as detailed below, and the position of $h \equiv 0$ at the top of the droplet is arbitrary but convenient.

Alternatively, $P_{F1i} - P_{F2i}$ can be determined from the Young–Laplace relation

$$P_{F1i} - P_{F2i} = \gamma(k1_i + k2_i) \quad (2)$$

where $k1_i$ and $k2_i$ are the principal curvatures of the droplet interface at depth $h_i$. Further, for an axisymmetric interface, $k1_i$ and $k2_i$ can be determined from local interfacial geometry (Figure 1A)[1,3]

$$k1_i = \mathrm{d}\theta_i/\mathrm{d}s \quad (3)$$

and

$$k2_i = \frac{1}{R2_i} = \sin\theta_i/R2_{Hi} \quad (4)$$

where $\theta_i$ is the angle between the interfacial tangent at $h_i$ and the horizontal; *s* is the arc length variable; $R2_i$ is the perpendicular distance between the interfacial tangent at $h_i$ and the central axis of the droplet; and $R2_{Hi}$ is the horizontal radius of the droplet at $h_i$. Combining eqs 1 and 2 yields

$$(\rho_{F1} - \rho_{F2})gh_i = -(P_{F1o} - P_{F2o}) + \gamma(k1_i + k2_i) \quad (5)$$


https://doi.org/10.1021/acs.langmuir.5c02838
Langmuir 2025, 41, 23096−23108

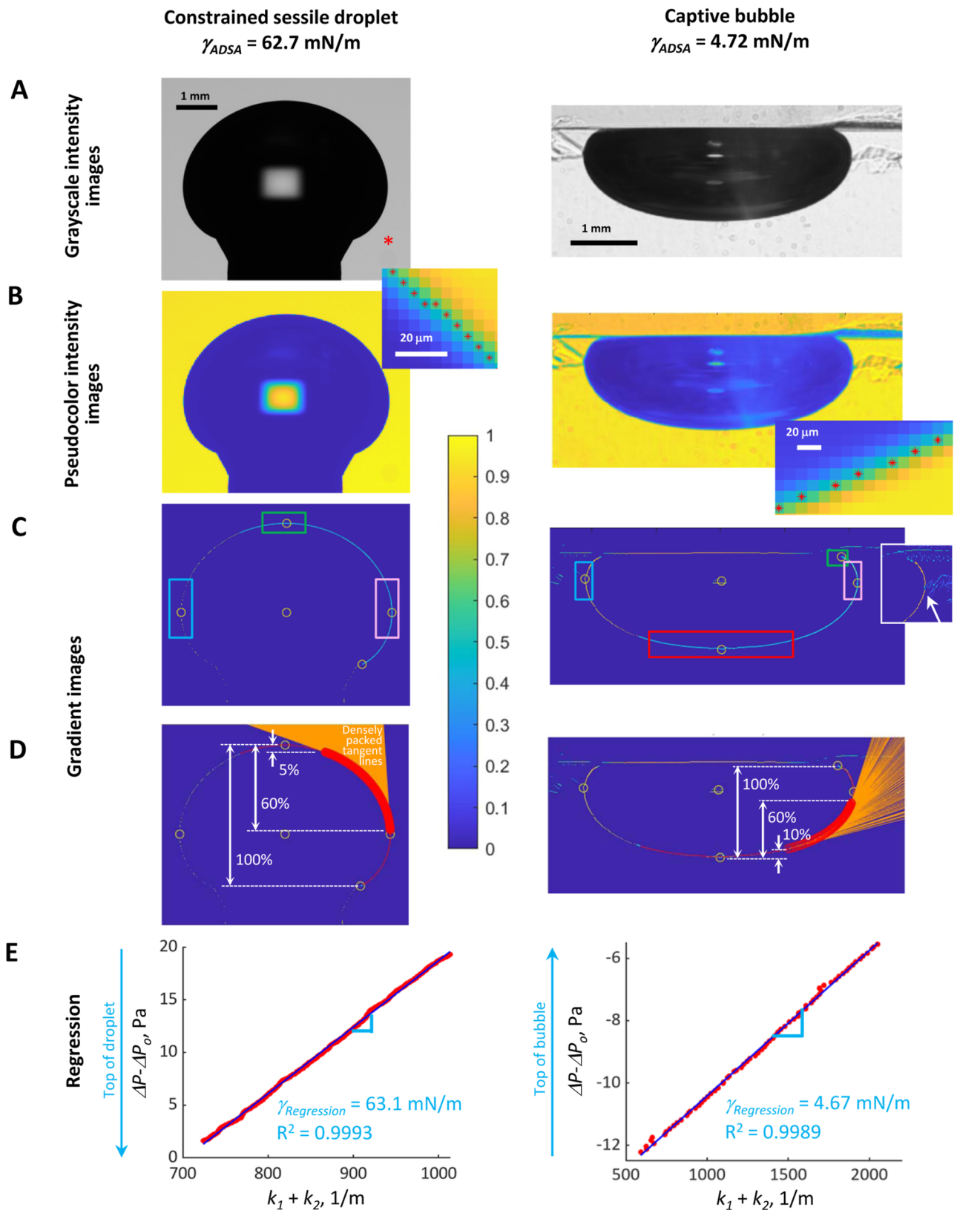


**Figure 2.** Regression-based surface tension determination algorithm. (A) Images of a constrained sessile droplet (CSD; left, 0.004 mm/pixel) and a captive bubble (right, 0.01 mm/pixel) with dipalmitoyl phosphatidylcholine (DPPC) monolayers, for which axisymmetric drop shape analysis (ASDA)-determined surface tension, $\gamma_{ADSA}$, is listed. In the CSD image, the red asterisk marks the elevation of the pedestal surface. (B) Pseudocolor versions of images from (A) following the normalization of intensity values to range of 0−1 and Gaussian smoothing. In insets, red asterisks mark pixels detected by subsequent Canny edge detection. Central color scale, ranging from 0 to 1, applies to images of (B−D) for intensity and gradient. (C) Maximal gradient magnitude images with blue background and yellow candidate-edge pixels identified by Canny edge detection plus thresholding. (Yellow edge pixels are faintly visible on left sides of the droplet/bubble interfaces. Edge pixels are continuous around



https://doi.org/10.1021/acs.langmuir.5c02838
Langmuir 2025, 41, 23096−23108

**Figure** 2. continued

the CSD and around most of the captive bubble, though not continuous at the bottom of the bubble. However, continuity of single-pixel-wide edge is not apparent due to the resolution of figures.) Inset of bubble image shows that edge detection alone, without thresholding, fails to isolate the bubble interface (white arrow). Colored boxes indicate areas selected with the mouse around top (green), left (cyan), right (pink), and bottom (red, bubble only) edge pixels. Program automatically finds extreme edge pixels (yellow circles) within boxes and averages extreme left and right edge pixels to obtain the central pixel (additional yellow circle). Edge pixels are sequenced, starting to left of center at top of the droplet or below agarose on right side of bubble and continuing to droplet-supporting surface or to left of center at bottom of bubble. Then, cyan line connects sequenced edge pixels. (D) Gradient images of (C) overlaid with truncated, filtered edge curves (red curves) that extend nearly but not all the way to the ends of cyan lines. Location of lowest curvature is at top of droplet, bottom of bubble. In an analysis region ranging from 5 or 10% to 60% of the vertical elevation away from location of lowest curvature, analysis points (red circles) are added atop red edge curve, and a tangent line (orange) is drawn at each analysis point. Density of analysis points and tangent lines is greater along the droplet than the bubble edge as the droplet is imaged at a higher resolution. (E) Regressions used to determine surface tension values $\gamma_{\text{Regression}}$. For droplet, $\Delta P$ increases with depth; thus, top is the location of the lowest $\Delta P - \Delta P_o$. For bubble, $\Delta P$ decreases with depth; thus, top is the location of the highest $\Delta P - \Delta P_o$.

**Table 1. Parameters Input to Program**

| | |
|---|---|
| parameters specified in first section of code that should be tailored to image being analyzed | |
| System | 1—Droplet; 2—bubble |
| InputImageFileName | Text string with image file name including extension, e.g. 'input file.tif' or 'input file.jpg' |
| OutputTextFileName | Text string with output file name including extension, e.g. 'output file.txt' |
| PrinterHeaderToOutputFile | 0—No, do not write column headers before writing data; 1—yes, write column headers |
| PrintDataToOutputFile | 0—No, do not write data to file; 1—yes, write data to file |
| SaveFigures | 0—No, do not save figure files; 1—yes, save figure files |
| GradThresh | Gradient threshold must be >0 and <1, is typically 0.2−0.6. Should be set to value greater than that of bright subphase pixels in gradient image and less than that of interface pixels in gradient image so that no structures in subphase connect to interface. Should also be set so that interfacial pixels are continuous in region of maximal diameter. In contrast, continuity of pixels in top region of droplet/bottom region of bubble is not essential. |
| CommentsPrevRun | Text string—add comments re. previous run, to be added to end of previous line in output file |
| CommentsCurrentRun | Text string—add comments re. run about to be performed, to be added to start of new line in output file |
| Wpix | Pixel width, in mm |
| ClickAtDropletBottom | For droplet: 0—no (must enter row number of droplet supporting surface in subsequent zBottom variable); 1—yes, be prompted to locate droplet bottom with mouse click in image. For bubble: N/A, parameter not used. |
| zBottom | For droplet, if ClickAtDropletBottom = 0, enter pixel row number (top row is row #1) of supporting surface in image. Should use row number from grayscale image, not pseudocolor image, as latter is cropped during smoothing by Gaussian convolution. |
| rhoL | Density of the less dense fluid, in kg/m$^3$ |
| rhoH | Density of the denser fluid, in kg/m$^3$ |
| parameters specified in second section of code that do not normally need to be modified | |
| dsFilter | 0.1—Arc length over which to spatially filter edge line, in mm |
| $f1$ | 0.05 —For droplet; 0.1 for bubble. Fraction of total interfacial elevation below top of droplet or above bottom of bubble at which to begin analysis region |
| $f2$ | 0.6—Fraction of total interfacial elevation below top of droplet or above bottom of bubble at which to end analysis region. |
| EnableCropping | 0—Not provided option of cropping regression curve; 1—provided option. Should set to 1 when using high $f2 > 0.6$, such that may encounter instability in curvature $k1$ near end of edge curve |
| dsKcap | 0.6—Maximum value of arc length $ds_K$ over which to determine curvature, in mm |
| dsKrange | 0.05—Range of $ds_K$ values, in mm, over which to obtain individual summed curvature values that will be averaged to obtain the employed summed curvature value for a given analysis point |
| $g$ | 9.81—Gravitational constant, in m/s$^2$ |

which may alternatively be written as

$$\Delta P_i - \Delta P_o = -\Delta P_o + \gamma(k1_i + k2_i) \quad (6)$$

Determining $\Delta P_i - \Delta P_o$ and $k1_i + k2_i$ at different depths, $h_i$, along the interface and plotting the former versus the latter will yield a relation with an intercept equal to $-\Delta P_o = -(P_{F1o} - P_{F2o})$ and a slope equal to $\gamma$. A linear relation would demonstrate that $\gamma$ was constant along the interface (Figure 1B).

**Algorithm.** Our algorithm for determining $\gamma$ by linear regression (for Matlab code, see Web site of corresponding author) may be applied to a grayscale intensity image of a droplet or bubble (Figure 2A).

*Overview.* We image a droplet or bubble, identify interfacial pixels by Canny edge detection, sequentially order the edge pixels to generate an edge line, and, to reduce the effect of pixelation, spatially filter the line to obtain a smoothed edge curve. From the set of all filtered edge points, we identify a subset as analysis points at which to determine $\Delta P_i - \Delta P_o$ and summed curvature. To determine the summed curvature at a given analysis point, we identify two supporting points before the analysis point and two supporting points after the analysis point with specified arc length interval $ds_K/2$ between sequential points. We use the supporting points to construct tangents to the interface. We determine tangent angles with respect to the horizontal, determine how tangent angle varies in the arc length direction, and use that information to calculate the summed curvature according to eqs 3 and 4. To further reduce the effect of pixelation, at each analysis point, we use as the summed curvature the average of individual summed curvature values calculated using a range of $ds_K$ values. We plot $\Delta P_i - \Delta P_o$ versus average summed curvature and observe whether the slope, $\gamma$, is constant.

*Grayscale Intensity Image and Preliminary Steps.* One begins by specifying in the code the variables in Table 1. In the case of a droplet, it is necessary to specify the elevation of the supporting surface and one has two options for doing so. First, one can set the variable ClickAtDropletBottom to 1 and will be prompted to click in the droplet image with a mouse at the elevation of the supporting surface (lateral position not important). Alternatively, one can set ClickAtDropletBottom to 0 and, in the code, set the variable zBottom


https://doi.org/10.1021/acs.langmuir.5c02838
Langmuir 2025, 41, 23096−23108

to the row number (top row is row #1) of the supporting surface. In this case, the row number is best determined by imaging the supporting surface prior to droplet deposition, determining surface elevation in the original grayscale version of that image and then keeping supporting surface elevation constant relative to camera elevation during subsequent droplet imaging. The latter option must be employed for a constrained sessile droplet (CSD) when there is no discontinuity in slope between the fluid−fluid interface and the angled pedestal edge.

*Pseudocolor Intensity Image.* Intensity values are normalized to span from 0 to 1. To reduce noise, Gaussian convolution is applied to the normalized intensity image.[4] A pseudocolor intensity image is then generated (Figure 2B, main images), along with a color scale.

*Gradient Image.* Canny edge detection is used to locate pixels at the interface. In a scheme adapted from Rachmawan,[4] the smoothed pseudocolor image is convolved separately with *x*- and *y*-Sobel filters to produce *x*- and *y*-gradient component matrices. From the gradient component matrices, resultants and arc tangents are calculated to determine gradient magnitude and direction, respectively, for each pixel. Gradient directions are binned into 45° categories. Then, the gradient magnitude of each pixel is compared with those before and after it in the local gradient direction. Gradient magnitudes that are not local maxima are suppressed. Gradient magnitude values are normalized from 0 to 1 and a pseudocolor gradient image depicting candidate edge pixels is generated (Figure 2C).

In the case of a turbid subphase, the gradient image contains bright pixels at the fluid−fluid interface and also often at the edges of structures in the subphase. Any such extraneous bright pixels that abut the interface (Figure 2C inset, white arrow) will cause problems with edge identification. Thus, the gradient image is thresholded at the level of the GradThresh parameter (Table 1), which should be set between the normalized gradient values of bright subphase pixels and brighter edge pixels. The result is a gradient image with a single-pixel-wide interfacial edge (faint yellow pixels on the left sides of interfaces in main Figure 2C images) surrounded by blue pixels with low/zero normalized gradient values. The yellow edge pixels need not be continuous over the full edge, for example, they may be discontinuous at the tops of droplets/bottoms of bubbles. To obtain an accurate result for $\gamma$, however, it is important that the edge pixels be continuous in the region of maximum diameter. Thus, with a turbid subphase, the GradThresh parameter should be specified at a low enough value that the edge pixels in this region are continuous. For interfaces that are surrounded by uniform-intensity fluids, the value of the GradThresh parameter is not critical but must be greater than zero because it is used in additional steps below.

*Identification of Extreme Edge Pixel Locations.* After detection of the interface, the user is asked to identify the locations of the extreme top, left, right, and bottom edge pixels. Identification of these extremes serves two purposes. First, they are used to locate the central axis, which is required for determining $k2$ (Figure 1A and eq 4). Second, as in the schematics of Figure 1, we use the right side of the interface for $\gamma$ determination. When sequencing right-side edge pixels, as detailed below, the extreme top, right, and bottom edge pixels are used as landmarks.

The user is asked to use the mouse to select boxes around the locations of the extreme interfacial edge pixels (Figure 2C). For a droplet, the user, having already identified the elevation of the supporting surface, selects the locations of the extreme top, left, and right pixels. Captive bubbles float against a dome of agarose, or alternative material, that obscures the location of the upper interface. Thus, for a captive bubble, the user selects a location around a portion of the interface just below the dome and on the right side of the bubble, where the first analysis pixel will be identified, and selects the locations of the extreme left, right, and bottom pixels. All selected regions should be wide enough to capture the extreme top, bottom, or side pixel as well as less extreme pixels before and after it along the interface. Once a particular region is selected, the extreme edge pixel in the region is automatically identified by an algorithm that makes use of the GradThresh parameter.

The extreme edge pixels are marked with open yellow circles in the gradient image (Figure 2C). The average of the extreme left and right edge pixels, the *x*-position of which is used as the location of the central axis, is also marked with a yellow circle. Correct positioning of the yellow circles should be verified visually. If the yellow circles are not appropriately located on, for example, a bubble interface, then the GradThresh parameter may need to be adjusted to separate the edge pixels from any bright pixels in the subphase. To obtain accurate surface area and volume values for a droplet (detailed below), the top circle should be visually verified to align with the central circle. To determine $\gamma_{\text{Regression}}$, perfect alignment of the top droplet circle or bottom bubble circle with the central circle is not essential. That said, significant misalignment may indicate that the interface is not axisymmetric, for example due to the supporting surface for a droplet not being level, or that the camera is not properly aligned.

Repeated analysis of the same image yields consistent $\gamma_{\text{Regression}}$ values. On repeated analysis of an image, the same automatically-detected extreme edge pixels are identified. Manual selection of a different droplet supporting-surface elevation or bubble top-pixel location causes a slightly different $\gamma_{\text{Regression}}$ value to be obtained. For example, four replicate analyses of a $\gamma_{\text{ADSA}}$ = 44.25 mN/m constrained sessile droplet image in which the identified supporting surface elevation is varied over a 15 pixel elevation range yield $\gamma_{\text{Regression}}$ of 44.18 ± 0.20 (standard deviation, SD) mN/m. Similarly, six replicate analyses of a $\gamma_{\text{ADSA}}$ = 52.60 mN/m captive bubble image with slightly varied top-pixel locating-box positions yield $\gamma_{\text{Regression}}$ of 54.14 ± 0.36 mN/m. The variance of such repeated $\gamma_{\text{Regression}}$ determinations is less than the error of the $\gamma_{\text{Regression}}$ method. Nevertheless, if one wishes to reproduce exactly the results of a prior run, then one can, at the end of the code section for extreme edge pixel identification, manually enter the extreme edge pixel coordinates that were found and written to an output data file in the previous run.

*Edge Pixel Sequencing and Edge Curve Generation.* We sequence edge pixels along the right side of the interface from the extreme top pixel to the supporting surface (droplet) or from the first edge pixel to the extreme bottom pixel (bubble) as follows. We identify the next-nearest edge pixel that has a gradient value exceeding the value of the GradThresh parameter. And then we proceed to sequence subsequent edge pixels. From the top pixel to the right-most pixel, the edge progresses rightward and downward, and we use the following search algorithm. With an initial search radius of one pixel, the next edge pixel is identified by searching first to the upper right of the current pixel and then proceeding downward along the right side of the current pixel, followed by leftward along the bottom of the current pixel. If necessary, the search radius is increased, one pixel at a time, until the next edge pixel is found. Beyond the right-most pixel, the edge changes direction to progress downward and leftward. Thus, between the right-most pixel and supporting surface elevation (droplet) or extreme bottom pixel (bubble), we change the search algorithm to the following. With an initial search radius of one pixel and again increasing the search radius as necessary, the next edge pixel is identified by searching first to the lower right of the current pixel and then proceeding leftward along the bottom of the current pixel, followed by upward along the left side of the current pixel.

To analyze as much of the vertical range of the interface as possible, it is desirable to locate analysis points near the top central point of a droplet and the bottom central point of a bubble. Doing so requires supporting points to be located to the left of the central axis. Thus, we use similar algorithms to start the edge curve to the left of the central axis for droplets and to extend the edge curve to the left of the central axis for bubbles.

Once all edge pixels have been sequenced, they are connected by a cyan line (right-hand side of interfaces in Figure 2C images). The edge pixels are also marked with red asterisks on the pseudocolor intensity image (Figure 2B, insets), enabling verification of appropriate edge location.

*Edge Curve Filtering.* The cyan connecting line of Figure 2C is jagged (visible in the enlarged images of Figure 4, below). To smooth the line, we filter the line with a window of constant differential arc length $ds_{\text{Filter}}$. That is, we replace the $x$ value of each edge pixel with


https://doi.org/10.1021/acs.langmuir.5c02838
Langmuir 2025, 41, 23096−23108

the average of the $x$ values of the edge pixels within a window stretching by the distance $ds_{Filter}/2$ in each direction along the edge. We do the same for the $y$ values. As linear pixel density varies along the edge, the number of pixels in the window is variable. As half of the $ds_{Filter}$ window is located to each side of the pixel being filtered, it is not possible at the start and end of the series of edge pixels to average over the full $ds_{Filter}$ window. To determine $\gamma_{Regression}$, the filtered edge curve is truncated by $ds_{Filter}/2$ at each end to avoid averaging over a window smaller than $ds_{Filter}$. The truncated filtered edge curve is plotted in red atop the gradient image (Figure 2D, red curves along the right sides of interfaces). The red edge curves largely obscure the cyan connecting lines of Figure 2C except that, due to the truncation, the red curves do not extend all the way to the ends of the cyan lines.

For droplets, an alternative nontruncated filtered edge curve is also generated by retaining all edge pixels and filtering over as much of $ds_{Filter}$ as possible. Differential arc lengths along the nontruncated filtered edge curve between the top central point and the supporting surface elevation are then used to determine surface area and volume by integration. For constrained sessile droplets with interfaces that end at a contact line at the pedestal rim, the determined surface area is the droplet surface area. For (unconstrained) sessile droplets with closed interfaces, which are continuous along and closely apposed to the supporting surface, the program does not currently determine complete surface area. For captive bubbles, given the disappearance of the top of the interface into the dome above, the present approach cannot be used to calculate surface area or volume. One could, however, use $\gamma_{Regression}$ and bubble width to find bubble height according to the method of Malcolm and Elliott and then, from bubble width and height, determine area and volume according to the method of Schoel et al.[2,5,6]

*Regression Analysis to Determine γ.* To determine $\gamma_{Regression}$, we use as analysis points edge curve points that are located within a specified fraction of the available vertical elevation of the interface (Figure 2D, red circles atop portions of the red edge curves). For droplets, the total vertical elevation between the top central point and the supporting surface is available. Relative to the top central point, which is the location of lowest summed curvature, we analyze edge curve points located between fractions $f1 = 0.05$ and $f2 = 0.60$ of the vertical distance to the supporting surface. For bubbles, the total available vertical elevation is that between the first edge curve point (selected below the dome material) and the bottom central point. And it is the bottom central point that is the location of lowest summed curvature. Because the total available bubble elevation is cropped at the level of the dome material, fractional elevations correspond to reduced absolute elevations. Thus, for bubbles, compared with droplets, we start the analysis region at a greater fractional distance away from the location of lowest summed curvature at the bottom central point. Relative to the bottom central point, we analyze bubble edge curve points located between fractions $f1 = 0.10$ and $f2 = 0.60$ of the vertical distance to the top point. The full rationale for these choices of analysis regions is discussed below.

At each analysis point, we must determine $\Delta P - \Delta P_o$ and summed curvature. We set depth $h$ equal to zero at the top/first pixel and, at each analysis point, calculate $\Delta P - \Delta P_o$ as $(\rho_H - \rho_L)gh$ for a droplet or $(\rho_L - \rho_H)gh$ for a bubble, where $\rho_L$ and $\rho_H$ are the densities of the lower and higher density fluids, respectively.

We determine the summed curvature as follows. Around each analysis point, to determine $k1 + k2$, we locate four supporting points at arc length intervals $ds_K/2$ (Figure 3). We use the supporting points to construct lines tangential to the interface (Figures 2D and 3). From the orientation of the tangent at an analysis point—i.e., the angle between the tangent and the horizontal—and the way that tangent orientation changes along the interface, we determine $k1$ and $k2$ according to eqs 3 and 4, respectively, as depicted in Figure 3.

Image pixelation introduces error into curvature determination by the above method. Thus, at each analysis point, to minimize error, we use a range of $ds_K$ values to determine the local summed curvature and then average the individual summed curvature values. In particular, for each of 100 equally spaced $ds_K$ values across the range, we identify the four supporting points at intervals $ds_K/2$ before

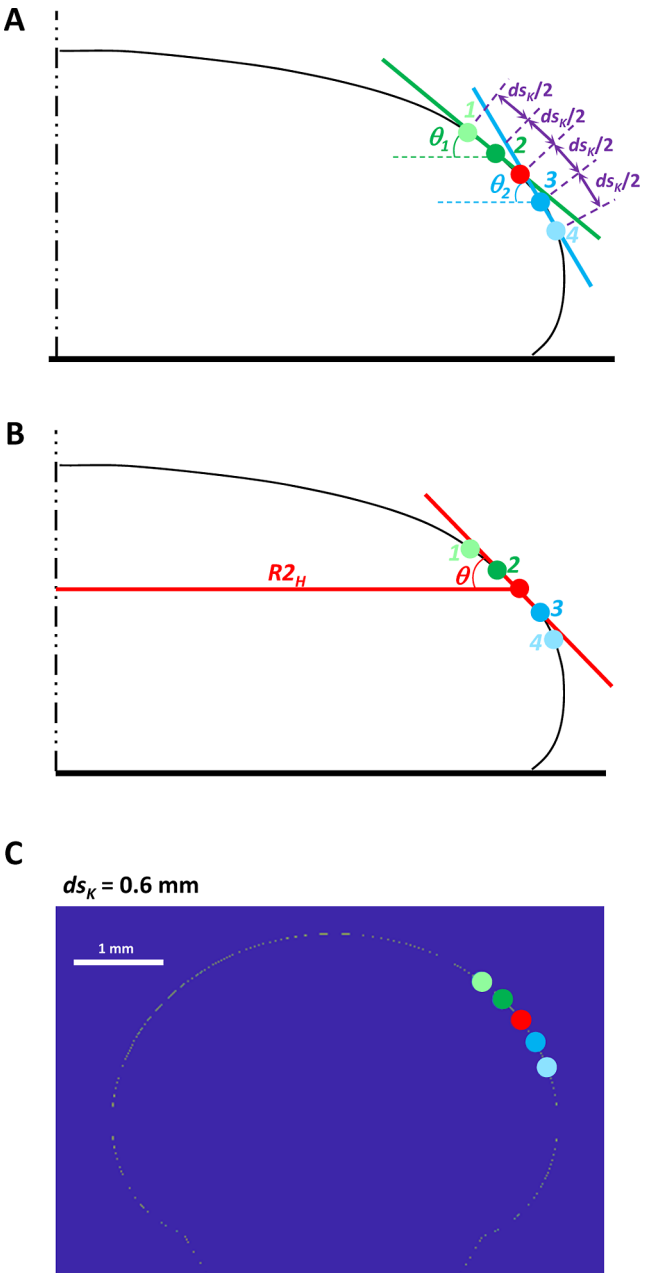


**Figure 3.** Determination of curvature. Principal curvatures $k1$ and $k2$ at an example analysis point (red) determined with the assistance of four supporting points (light green, green, cyan, and light blue) identified at arc length intervals $ds_k$ and $ds_k/2$ before and after the analysis point. (A) Curvature $k1$ is determined, according to eq 3, as $d\theta/ds = (\theta_2 - \theta_1)/ds_k$, where $\theta_1$ is the angle with respect to horizontal of the green line that is tangent to green point #2 and that is constructed between light green point #1 and the red analysis point, which are separated by arc length $ds_k$; $\theta_2$ is the angle with respect to horizontal of the cyan line that is tangent to cyan point #3 and that is constructed between the red analysis point and light blue point #4, which are separated by arc length $ds_k$; and $ds_k$ is also the arc length between green point #2 and cyan point #3. (B) Curvature $k2$ is determined, according to eq 4, as $\sin\theta/R2_H$, where $\theta$ is the angle with respect to horizontal of the red line that is tangent to the red analysis point and that is constructed between green point #2 and cyan point #3, which are separated by arc length $ds_k$; and $R2_H$ is the horizontal distance between the red analysis point and the central axis. (C) Supporting points for $ds_K = 0.6$ mm shown about an example red analysis point on the interface of a CSD for which $\gamma_{ADSA} = 62.7$ mN/m. Given the close packing of analysis points (Figure 2D), the


https://doi.org/10.1021/acs.langmuir.5c02838
Langmuir 2025, 41, 23096−23108

**Figure** 3. continued

supporting points for different analysis points (other red points, not shown on this figure), overlap.

and after the analysis point and calculate $k1$ and $k2$. Because only discrete points are available along the edge curve for use as supporting points, however, the 100 $ds_K$ values yield a limited number of different sets of supporting points. (At least one of the four supporting points must differ between two different sets of supporting points.) For each set of supporting points, we obtain a value for the summed curvature. We use the average of all individual summed curvature values for a given analysis point as the summed curvature value at that analysis point.

Empirically, we identify the following choices for the $ds_K$ values to be used. We determine summed curvature using a $ds_K$ range of 0.55−0.60 mm and 100 $ds_K$ values within the range. Near the ends of droplet edge curves and the starts of bubble edge curves, however, there is not sufficient room to locate supporting points at $ds_K$ = 0.60 mm before and after each analysis point. Therefore, we decrease $ds_K$ as necessary but still use a $ds_K$ range of 0.05 mm and 100 $ds_K$ values within the range. Further algorithmic details for analysis points located near the ends of edge curves are discussed below.

Across all analysis points, we plot $\Delta P - \Delta P_o$ versus $k_1 + k_2$ and perform a linear regression to determine surface tension (Figure 2E). Parameters used and results obtained can be written to a data output file.

**Experimental Methods.** For droplet experiments, we image a constrained sessile droplet with a DPPC monolayer atop a pedestal. Similar to a published design,[7] we use a 0.132 in diameter pedestal surface with a 60° edge angle and a 0.021 in diameter central hole (Columbus Machine Works, Columbus, OH) through which we add or remove subphase liquid with a connected syringe. We illuminate with a collimated LED light source (BL2 × 2-CL-B-24-ILD-BC-PS, Metaphase Lighting Technologies, Bristol, PA) located 20 cm behind the pedestal. We image with a monochromatic camera (EO-50232M, 2456 × 2054 pixels, 3.45 $\mu$m pixel size, Edmund Optics, Barrington, NJ), a telecentric lens with an 11 cm focal distance (62-901, 0.9X LF PlatinumTL Telecentric, Edmund Optics), and uEye image capture software (IDS, Stoneham, MA). We establish a 40 $\mu$L droplet of normal saline on the pedestal at room temperature, 20 ± 1 °C, and capture an image. We deposit 37 ng of DPPC in 3 $\mu$L of chloroform and wait for the chloroform to evaporate. We use the syringe to alter subphase volume/interfacial surface area, and thus surface tension. And we image the droplet over a range of surface tensions.

For bubble experiments, we image a captive bubble with a DPPC monolayer using previously described methods.[6,8,9] We establish a bubble in buffered normal saline at room temperature, 23 ± 1 °C, and capture an image. We spread a solution of DPPC in chloroform on the surface of the bubble and the DPPC forms a monomolecular film. Exhaustive exchange of the subphase removes the chloroform.[8] We inject saline into the subphase to decrease the bubble to different volumes/surface areas and thus compress the monolayer to lower surface tensions. And we image the bubble over a range of surface tensions.

In an alternative series of bubble experiments, we establish a bubble in water at room temperature of 23 ± 1 °C and do not spread lipid. We compress the clean bubble so that the surface area decreases by 54%. We image the bubble over the range of surface areas.

**Tuning and Statistical Methods.** We initially analyze two droplet and three bubble images (identified in Figure 7A, below) and, by comparison of $\gamma_{Regression}$ to $\gamma_{ADSA}$, identify appropriate regression-algorithm parameters (Table 1, bottom section). Then, for additional droplet and bubble images, we use the identified parameters to determine $\gamma_{Regression}$ and we also determine $\gamma_{ADSA}$.

We assess the correlation between regression-method results and those of ADSA, reporting intercept and slope [95% confidence intervals], as well as coefficient of determination, $R^2$. We determine the accuracy of the regression method by calculating

$$\Delta\text{Error} = (\text{regression-determined value}) - (\text{ADSA-determined value}) \quad (7)$$

e.g., $\gamma_{Regression} - \gamma_{ADSA}$, and

$$\%\ \Delta\text{Error} = \frac{\Delta\text{Error}}{\text{ADSA-determined value}} \times 100 \quad (8)$$

e.g., $[(\gamma_{Regression} - \gamma_{ADSA})/\gamma_{ADSA}] \times 100$. We present plots for ΔError and % ΔError. And we report mean ± SD for the absolute values of the two error metrics, |ΔError| and |% ΔError|.

## RESULTS AND DISCUSSION

We first consider aspects of the methodology for determining $\gamma_{Regression}$. Next, we compare regression-determined surface tension values to those determined by ADSA. Finally, we discuss ramifications of the new approach.

**Methodologic Considerations.** Two methodologic topics merit consideration: those of pixelation and of curvature determination near the top and bottom of the edge curve. The topics are interrelated.

*Pixelation Effects.* Working with pixelated images introduces inaccuracies into the $\gamma_{Regression}$ method. Due to image pixelation, the cyan line that connects yellow edge pixels is jagged (Figure 4). Smoothing the edge line reduces but does

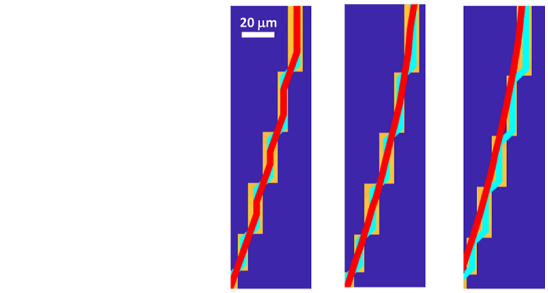


**Figure 4.** Edge line filter width. Three images are of the same edge pixels (yellow) from the same gradient image of the same $\gamma_{ADSA}$ = 13.4 mN/m captive bubble with a DPPC monolayer. Pixels in each version of the image are connected by the same cyan line. The cyan line is spatially filtered with three different values of arc length window $ds_{Filter}$ to produce three alternative, smoothed red edge lines.

not eliminate the effect of pixelation, and an appropriate smoothing approach must be identified. With a low $ds_{Filter}$ of 0.01 mm, the filtered red edge curve is not smooth. With a high $ds_{Filter}$ of 0.3 mm, the filtered red edge curve is smooth but, instead of overlying the yellow edge pixels and cyan connecting line, is displaced toward the center of the curvature. With an intermediate $ds_{Filter}$ of 0.1 mm, the filtered red curve is relatively smooth and overlies the yellow edge pixels and the cyan connecting line. In Figure 2, the droplet and bubble are imaged with different cameras. The droplet has a width of 5 mm, pixel width of 0.004 mm (1250 pixels across the droplet width), and $\gamma_{ADSA}$ of 63 mN/m. The bubble has a width of 4 mm, pixel width of 0.01 mm (400 pixels across the droplet width), and $\gamma_{ADSA}$ of 5 mN/m. Across these varied conditions, setting $ds_{Filter}$ to 0.1 mm provides an edge curve comparable to that in the central panel of Figure 4. We set $ds_{Filter}$ to 0.1 mm for all analyses.


https://doi.org/10.1021/acs.langmuir.5c02838
Langmuir 2025, 41, 23096−23108

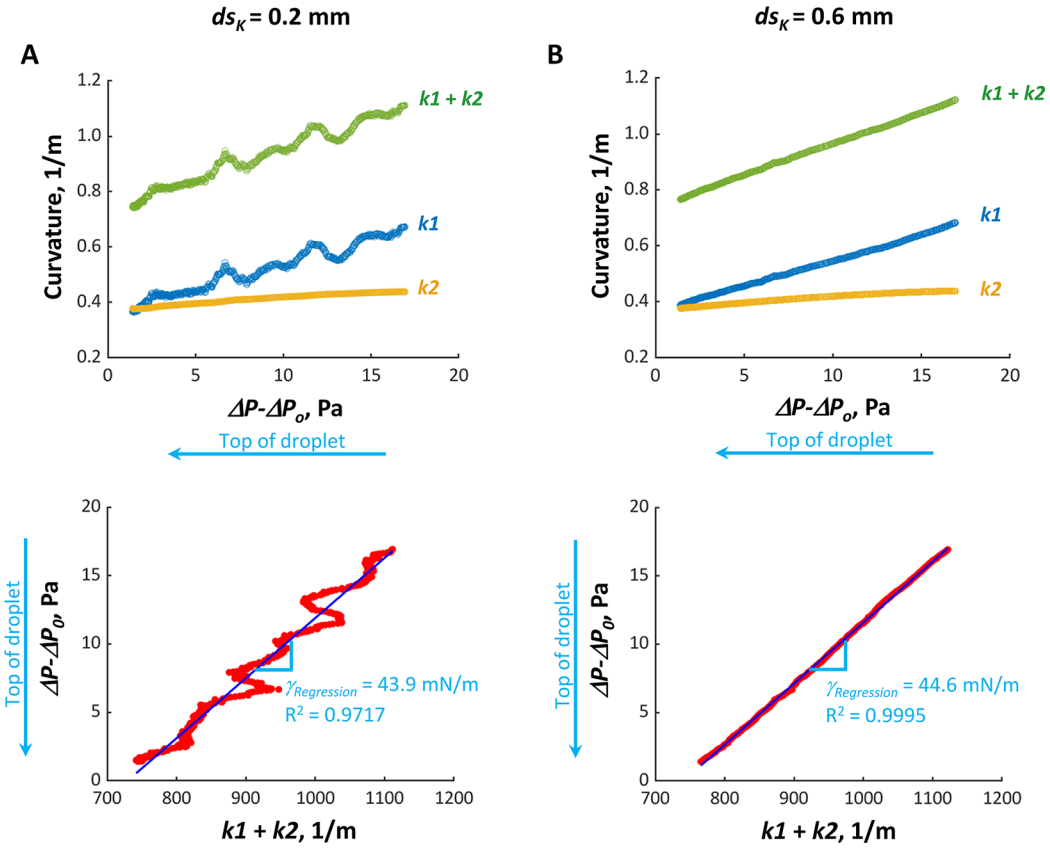


**Figure 5.** Curvature. Data are for $\gamma_{ADSA}$ = 44.3 mN/m captive sessile droplet. (A) When $ds_K$ is small, curvature $k1$ oscillates with position along the edge curve for reasons detailed in text. Consequently, the plot of $\Delta P - \Delta P_o$ vs $k1 + k2$ oscillates about the regression line. (B) When $ds_K$ is larger, oscillation disappears. For the droplets and bubbles analyzed, the relation between either $k1$ or $k2$ and hydrostatic pressure offset from top of droplet, $\Delta P - \Delta P_o$, can be nonlinear. However, the relation between the sum $k1 + k2$ and $\Delta P - \Delta P_o$ is linear. In the plots of this figure, the values for $k1$, $k2$, and the sum $k1 + k2$ are each the average of the different values determined from the different sets of supporting points identified over the utilized $ds_K$ range. As the hydrostatic pressure offset is a multiple of elevation, the relation between $k1 + k2$ and elevation is linear.

We calculate curvatures over an arc length interval of $ds_K$ (Figure 3). This process is also affected by pixelation. As the pixelated edge line traverses the image field, the line periodically jumps back and forth across the true edge position. Smoothing the pixelated edge line reduces but does not eliminate such jumps. Using a small $ds_K$ value leads to curvature calculation from local pixel locations that, at periodic positions along the edge and despite smoothing, are biased toward the inside (toward the center of curvature) or outside of the true edge curve, which should result in overestimation or underestimation, respectively, of curvature. This periodic overestimation/underestimation of curvature causes $k1$ to oscillate along the interface and, in turn, the plot of $\Delta P - \Delta P_o$ vs $k1 + k2$ to oscillate about the average, linear slope (Figure 5A). Using a larger $ds_K$ value essentially eliminates such oscillations (Figure 5B).

Further, using a single $ds_K$ value subjects curvature determination to local pixelation patterns. To minimize the effect of such local patterns, we use an average of individual summed-curvature values, each determined using a slightly varied $ds_K$ value. For a given analysis point, each $ds_K$ value used must correspond to a different set of supporting points. The number of different sets of supporting points available is limited by image resolution and thus local edge point density along the interface. For droplets imaged with a 0.004 mm pixel width, the number of different sets of supporting points used is typically about 30 but can be as low as 22. For bubbles imaged with a 0.01 mm pixel width, the number of different sets of supporting points used is typically about 10 but can be as low as 3 for select analysis points under low-$\gamma$ conditions. Despite these differences, we find error to be comparable for the two sets of experiments (see Algorithm Evaluation section, below). Both the use of relatively large $ds_K$ values and averaging individual summed curvatures determined from slightly varied $ds_K$ values improve the accuracy of curvature determination, thus improving the accuracy of surface tension determination.

*Curvature Determination at Top and Bottom of Edge Curve.* We typically determine $\gamma_{Regression}$ using the analysis points located between 5 or 10% and 60% of the elevation range (Figure 2D), but the range can be modified by altering parameters $f1$ and $f2$ (Table 1). Beyond the typical analysis range, the summed curvature can become unstable near the top and bottom of the vertical range. Figure 6 shows an example in which regression analysis is performed over 0−96% of the elevation range of a droplet. As $\Delta P$ increases downward for droplets but upward for bubbles, the analysis points in the lower left of the regression plots, at low $\Delta P$ and low summed curvature, are near the top centers of droplets and near the bottom centers of bubbles (Figures 2E and 6A). Figure 6A,B (yellow box) shows that using too low of a fraction $f1$ reduces the accuracy of $\gamma_{Regression}$ due to the inclusion of analysis points that are very close to the central axis, for which computational determination of $k2$ is unreliable. On encountering this


https://doi.org/10.1021/acs.langmuir.5c02838
Langmuir 2025, 41, 23096−23108

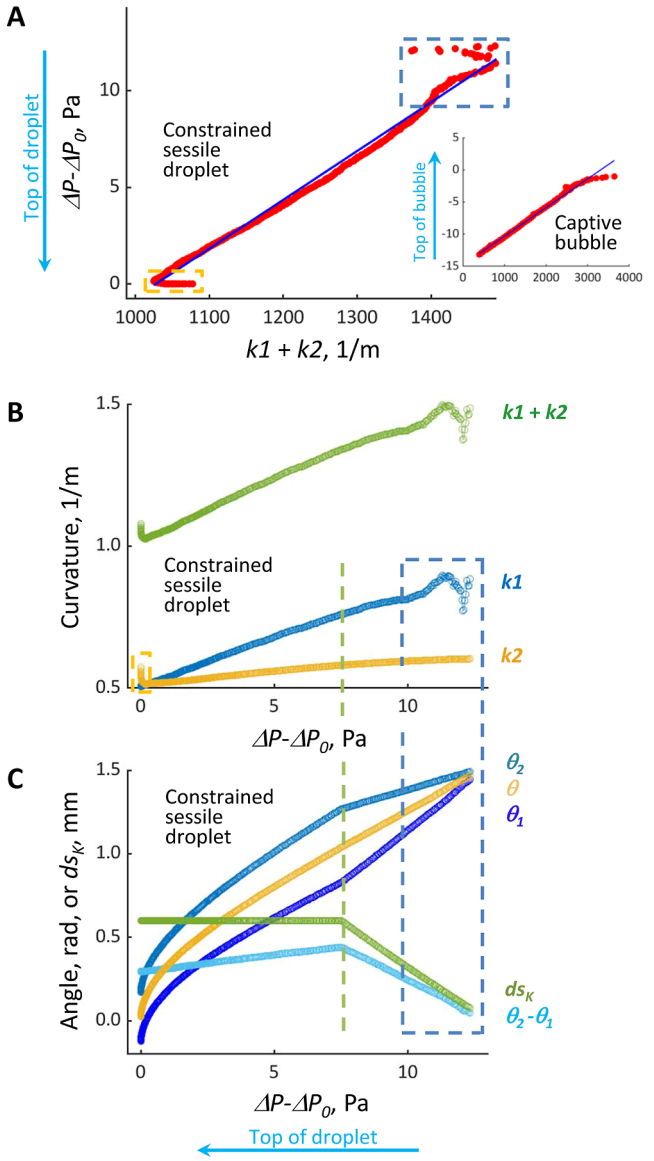


**Figure 6.** Curvature determination effects at top and bottom of edge curve. Results shown for regression analysis performed over 0−96% of vertical elevation range of $\gamma_{ADSA}$ = 22.9 mN/m CSD. (A) Regression curve. Inset is a regression curve for analysis performed over 3−96% of vertical elevation range of $\gamma_{ADSA}$ = 4.7 mN/m captive bubble. (B) Curvatures plotted vs hydrostatic offset in $\Delta P$ from that at the top of the droplet. (C) Tangent angles and $ds_K$ plotted vs hydrostatic offset in $\Delta P$ from that at the top of the droplet. Additional details provided in text.

problem, one should increase the value of $f1$ to, e.g., 0.05 for droplet images or 0.10 for bubble images.

At the upper right of the regression plots, at high $\Delta P$ and high summed curvature, the analysis points are near the end of the edge curve by the supporting surface for droplets or the dome material for bubbles. As the analysis points approach the end of the edge curve, there is no room to locate a supporting point at $ds_K$ = 0.6 mm beyond each analysis point. Thus, as analysis points near the end of the edge curve, $ds_K$ is progressively reduced (Figure 6C). The reduction in $ds_K$ affects several parameters, as seen to the right of the dashed green line in Figure 6C. It alters the relations between $\theta_1$ and $\theta_2$ (Figure 3A) and elevation, though not that between $\theta$ (Figure 3B) and elevation. This difference is because, as $ds_K$ decreases for successive analysis points along the edge curve, the interval over which $\theta_1$ (or $\theta_2$) is determined is shortened asymmetrically, with supporting point 1 (or supporting point 4) always moving closer to the analysis point. In contrast, the interval over which $\theta$ is determined is shortened symmetrically, with supporting points 2 and 3 both moving the same distance closer to the analysis point. The changes in slopes of the $\theta_1$- and $\theta_2$-elevation relations reduce the difference $\theta_2 - \theta_1$ (Figure 6C), but they do so proportionately to the decrease in $ds_K$ such that the ratio of eq 3 remains constant and $k1$ is not initially affected (Figure 6B, $k1$ in section between the green line and blue box).

As the analysis points get closer to the end of the edge curve, $k1$ becomes unstable. For the droplets we analyze, the $k1$ vs $\Delta P - \Delta P_o$ and regression plots often exhibit oscillations that we attribute to the pixelation effect with low $ds_K$ value in the region of greatest summed curvature (Figures 5A and 6A,B, blue boxes). For the bubbles we analyze, the regression, rather than oscillating, tends to veer toward a lower slope (Figure 6A inset). While a lower slope at the top of the regression for a bubble could indicate a lower $\gamma$ in the region, the decrease in slope is dramatic, to ∼20% of that of the rest of the interface. This difference is not supported by ADSA of subregions of bubble interfaces, which shows no marked difference in $\gamma$ between the top portions of interfaces and the remaining portions of interfaces. We interpret that the difference between the droplets and bubbles that we analyze is attributable to the different pixel resolutions of the images with which we capture each. The coarser resolution of bubble images should reduce the oscillation frequency, and the drift of the bubble regression slope may comprise the initial portion of an oscillation.

Typically, oscillations/nonlinearity develop only in the last ∼20% of the vertical elevation range before the end of the edge curve. However, occasionally, they develop in the last 40% of the range. And, in the cases for which there are no oscillations in the last 40% of the range, ending the analysis region at 60% of the vertical range (omitting the last 40%) generates as accurate $\gamma_{Regression}$ values as ending the analysis region at 80% of the vertical range (omitting the last 20%). Thus, for simplicity and reliability, we end the analysis region at 60% of the vertical range. However, the range can be extended as desired. Additionally, one can optionally set parameter Crop (Table 1) to 1 and increase parameter $f2$, which specifies the end of the analysis range (e.g., $f2$ = 0.96 for the analysis of Figure 6). In this case, the program initially performs the regression for the specified vertical range. Then, the user is given the option of drawing a box around analysis points at the upper right end of the regression plot (Figure 6A, blue box) that should be omitted (enter "y" to elect to crop) or of accepting the regression as is (enter "n" to elect not to crop). If cropping is elected, then analysis points above the lower boundary of the selected region are omitted, the regression is rerun, and a new $\gamma_{Regression}$ value is determined. In the case that cropping is employed, data are not written to the output file until after the analysis region is cropped. So long as the final analysis region does not include points within unstable regions near the end points of the edge curve, the $\gamma_{Regression}$ value obtained is reliable.

We note that the difference between ending the analysis region at 60 vs 80% of the elevation range coincides with ending it before vs after the elevation of maximal diameter. As detailed above, accurate computational summed curvature determination requires the presence of continuous edge pixels


https://doi.org/10.1021/acs.langmuir.5c02838
Langmuir 2025, 41, 23096−23108

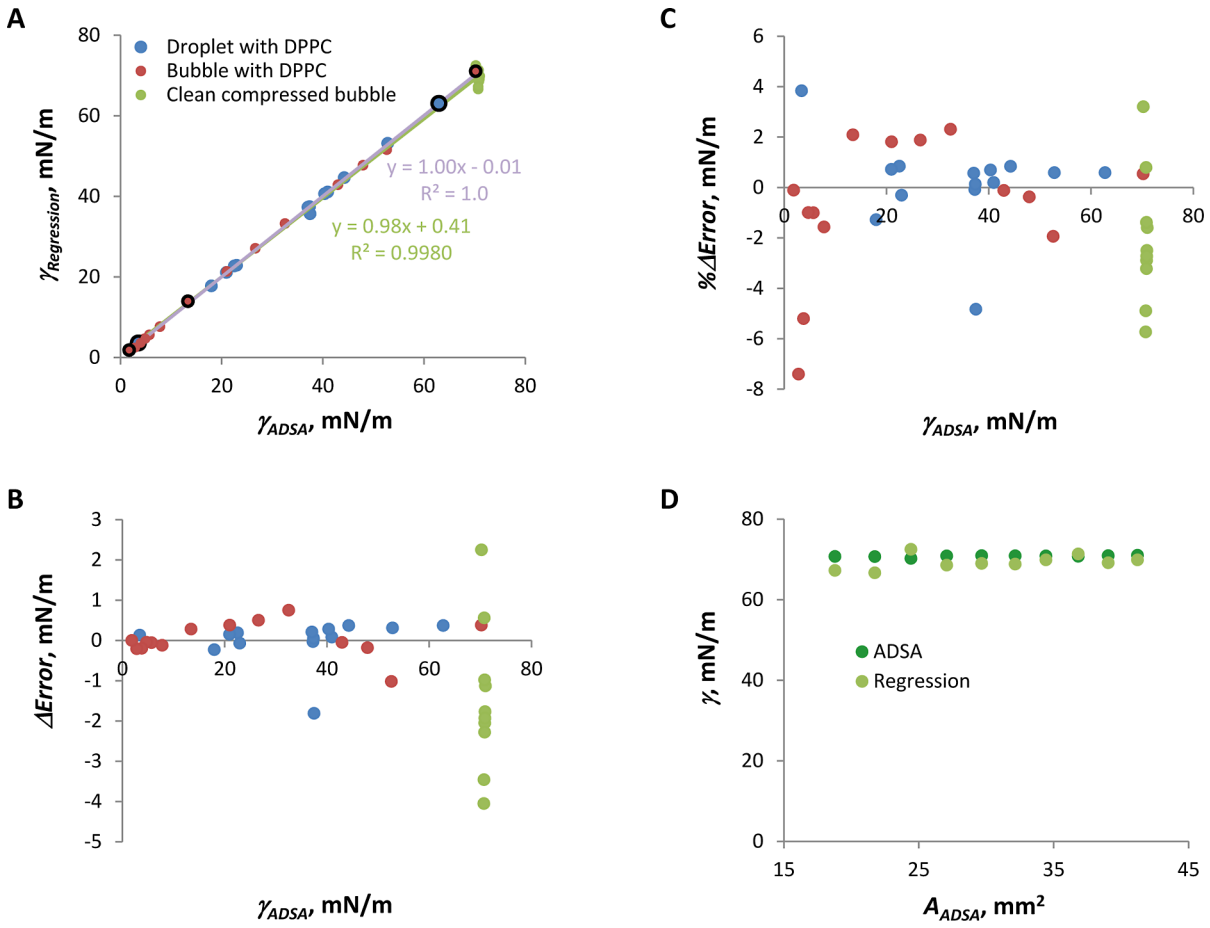


**Figure 7.** Accuracy of $\gamma_{Regression}$ method. (A) Correlation between $\gamma$ determined by regression method and ADSA. Appropriate parameters for $\gamma_{Regression}$ analysis identified by initial analysis of two droplet and three bubble images. Data points for those images are outlined in black. Droplet group includes single data point for which $\gamma_{Regression}$ is determined with use of the ElectToCrop option to reduce $f2$ below 0.60. Purple line is fit to combined data for droplet and bubble with DPPC monolayers (blue and red groups). Green line is fit to combined data from all three groups. (B) Error metric plotted vs $\gamma_{ADSA}$. (C) % Error metric plotted vs $\gamma_{ADSA}$. (D) For compression of a bubble with a clean interface, $\gamma$ determined by the regression method or ADSA plotted vs interfacial area determined by ADSA.

**Table 2. Correlations for Surface Tension Error Analysis**[a]

| | $\gamma_{Regression}$ vs $\gamma_{ADSA}$ | \|ΔError\| vs $\gamma_{ADSA}$ | \|% ΔError\| vs $\gamma_{ADSA}$ |
|---|---|---|---|
| | droplet and bubble with DPPC monolayers, combined | | |
| intercept | −0.01 [−0.36, 0.33], N.S. | 0.13 [−0.13, 0.38], N.S. | 2.7 [1.5, 3.8], $p < 0.001$ |
| coefficient | 1.0 [0.99, 1.0], $p < 0.001$ | 0.01 [0.01, 0.01], N.S. | −0.04 [−0.07, −0.01], $p < 0.05$ |
| $R^2$ | 1.0 | 0.10 | 0.18 |
| | droplet with DPPC monolayer, bubble with DPPC monolayer and clean bubble, all combined | | |
| intercept | 0.41 [-0.29, 1.1], N.S. | −0.28 [-0.76, 0.20], N.S. | 1.9 [0.71, 3.0], $p < 0.005$ |
| coefficient | 0.98 [0.97, 1.0], $p < 0.001$ | 0.03 [0.02, 0.04], $p < 0.001$ | 0.00 [-0.02, 0.03], N.S. |
| $R^2$ | 1.0 | 0.42 | 0.00 |

[a]Linear regression metrics reported with [95% confidence intervals]. Abbreviations: N.S.—not significant; $R^2$—coefficient of determination.

in this region. (This condition is necessary even when the analysis region ends before the elevation of maximal diameter, as supporting points are still generally located at and beyond the elevation of maximal diameter.) So long as this condition is met, the regression is linear and stable up to $f2$ of 0.80 in the majority of cases, e.g., Figure 6A. This result demonstrates that the algorithm remains accurate around the reversal of the edge curve at the elevation of maximal diameter.

**Algorithm Evaluation Results.** For the droplets and bubbles that we analyze, we find that the sum $k1 + k2$ varies linearly with $\Delta P - \Delta P_o$ (Figure 5B); as $\Delta P - \Delta P_o$ varies linearly with elevation, so does $k1 + k2$ vary linearly with elevation. Consequently, the assumption that $\gamma$ is constant is valid for these interfaces, and $\gamma$ can be determined by linear regression (Figure 2E).

We plot $\gamma_{Regression}$ vs $\gamma_{ADSA}$ (Figure 7A). Considering just the droplet and bubble with DPPC monolayers (blue and red groups, each of which includes a single clean-interface data point), linear regression yields an intercept of −0.01, a slope of 1.0, and an $R^2$ value of 1.0 (Figure 7A and Table 2). The |ΔError| for $\gamma_{Regression}$ is almost always ≤1 mN/m and the |% ΔError| is on the order of 2% (Figure 7B,C and Table 3).



https://doi.org/10.1021/acs.langmuir.5c02838
Langmuir 2025, 41, 23096−23108

Table 3. Error values[a]

| | \|ΔError\| | \|% ΔError\| |
|---|---|---|
| droplet with DPPC monolayer | 0.31 ± 0.45 | 1.1 ± 1.4% |
| bubble with DPPC monolayer | 0.30 ± 0.29 | 2.0 ± 2.0% |
| droplet and bubble with DPPC monolayers, combined | 0.30 ± 0.37 | 1.5 ± 1.8% |
| bubble with clean interface | 2.05 ± 1.07 | 2.9 ± 1.5% |
| all data, combined | 0.76 ± 0.99 | 1.9 ± 1.8% |

[a]Values presented as mean ± standard deviation.

The |ΔError| does not correlate with $\gamma_{ADSA}$ (Table 2). Consequently, the |% ΔError|, in which |ΔError| is normalized by $\gamma_{ADSA}$, correlates inversely with $\gamma_{ADSA}$ (Figure 7C and Table 2).

For the compressed bubble with a clean interface, $\gamma_{Regression}$ varies more than $\gamma_{ADSA}$ and increasingly so at a lower surface area (Figure 7D). Reducing the surface area with a fixed pixel size effectively reduces imaging resolution. For the images of the interfaces with DPPC monolayers, there are at least 400 pixels across the width of the droplet or bubble; for the smallest compressed, clean bubble, there are 260 pixels across the width. The |ΔError| for the clean bubble is ∼1 mN/m with at least 360 pixels across the bubble width, increases to ∼2 mN/m for 300−360 pixels across the bubble width, and increases to ∼4 mN/m for 260−300 pixels across the bubble width. Given the relatively low image resolution in this data group, the |ΔError| and |% ΔError| are relatively high (Figure 7B,C and Table 3). Thus, when these data are combined with those of the groups with DPPC monolayers, correlations are altered (Figure 7A and Table 2). Imaging compressed clean interfaces with a higher-resolution camera should improve accuracy at low surface area.

For the constrained sessile droplet with a DPPC monolayer, we also assess the correlation between the surface area, $A$, determined by the regression method and by ADSA (Figure 8). Linear regression yields an intercept of 0.14 [−0.01, 0.29] (N.S.), a slope of 0.96 [0.95 to 0.96] ($p < 0.001$), and an $R^2$ value of 1.00. The |ΔError| and |% ΔError| values for $A$ are 1.12 ± 0.58 mm$^2$ and 3.5 ± 0.9%, respectively.

**Implications of Regression Method.** We compare the new regression method to existing virtual methods, consider the physical meaning of $\gamma$ being constant along the interface, and consider potential extension of the new method to more complex scenarios.

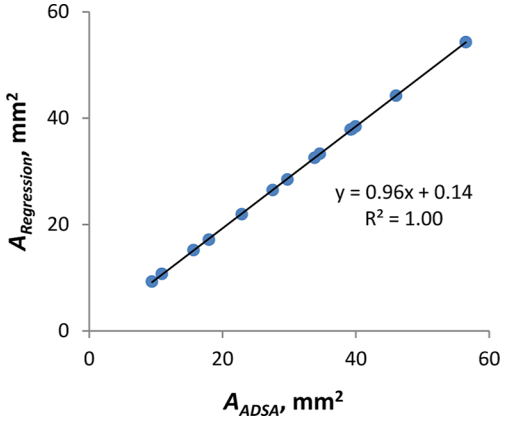


**Figure 8.** Accuracy of surface area determination by regression method. Correlation between the surface area, $A$, determined by regression method and ADSA for a CSD with a DPPC monolayer compressed to different degrees.

*Comparison to Existing Virtual Methods.* Analysis of the variation in curvature with elevation along an interface is a virtual approach that does not require physical contact with the interface. The lack of contact is a strength of such methods. Approaches that require physical contact can be challenging to implement, particularly under extreme conditions such as low $\gamma$, high temperature, or high hydrostatic pressure.[10] For example, barriers used to compress surfactant monolayers often nucleate monolayer collapse. Further, as low $\gamma$ is frequently assessed by the analysis of closed droplets or bubbles,[3,10,11] the ability to analyze closed interfaces is important. Thus, we consider our new regression-based method in relation to other virtual $\gamma$-determination methods that can be applied to closed interfaces—the method of Malcolm and Elliott and ADSA.

The method of Malcolm and Elliott enables $\gamma$ determination from only two parameters, height and maximal diameter.[2] The approach is sufficiently fast computationally that it has been used to determine $\gamma$ in real time during rapid compression.[11] However, the approach can be applied only to closed interfaces, requires visualization of the complete interface for the determination of height and diameter, and assumes constant $\gamma$. For bubbles floating against a dome that obscures the upper interface, visualization of the complete interface is challenging.[6]

ADSA comprises numerical integration of parametric equations and optimization of the fitting of a theoretical curve to an experimentally-captured interfacial contour.[1,3] Due to the optimization, ADSA is the most accurate of the virtual approaches. The method is also more flexible than that of Malcolm and Elliott in that it can be applied to all or a portion of axisymmetric interfaces that are closed or that have a contact line. That said, ADSA is complex to implement and assumes $\gamma$ to be constant.

The present regression method, like ADSA, can be applied to all or a portion of axisymmetric interfaces that are closed or that have a contact line. Beyond that similarity, the regression method is less precise than ADSA but has its own advantages. The regression method does not assume constant $\gamma$. Further, the regression method is simple in concept; conveys physical understanding, as detailed below; and has the potential to be extended to nonaxisymmetric interfaces, as also detailed below.

*Physical Interpretation.* Regression-based analysis is uniquely aligned with the direction of the physical influence of gravity. It is implicit in the Young−Laplace relation that if $\gamma$ is constant, then the summed curvature must vary linearly with elevation. Our results show that, for the interfaces we analyze, the summed curvature varies linearly with $\Delta P - \Delta P_o$ and thus with elevation. That is, gravity-induced variation in $\Delta P$ is balanced by a proportionate variation in curvature.

This physical understanding of how the summed curvature varies with elevation cannot be inferred visually from meridian images, in which only one of the two principal curvatures is apparent. Further, it is obscured by the Malcolm and Elliott and ADSA approaches, as curvature is subsumed into the differential equations of those approaches. The relation between summed curvature and elevation has not previously, to our knowledge, been elucidated.

For the droplets and bubbles that we analyze, the relation between $\Delta P - \Delta P_o$ and summed curvature is linear and $\gamma$ is constant. For alternative interfaces, the relation might be


https://doi.org/10.1021/acs.langmuir.5c02838
Langmuir 2025, 41, 23096−23108

nonlinear. A nonlinear relation would mean that $\gamma$ varied along the interface.

*Potential for Extension to Nonaxisymmetric Interfaces.* The present method utilizes axisymmetry for the determination of the out-of-plane curvature $k2$, according to eq 4. A different method of curvature determination, however, could enable regression-based $\gamma$ determination to be extended to nonaxisymmetric interfaces. If the interface could be mapped locally around each of a series of vertically-spaced analysis points by an explicit surface $z = f(x,y)$, then the summed curvature at each analysis point could alternatively be determined as

$$k1 + k2 = \frac{(1 + f_x^{\,2})f_{yy} - 2f_x f_y f_{xy} + (1 + f_y^{\,2})f_{xx}}{(1 + f_x^{\,2} + f_y^{\,2})^{3/2}} \tag{9}$$

where subscripts indicate partial derivatives, e.g., $f_x = \frac{\partial z}{\partial x}$ and $f_{xy} = \frac{\partial^2 z}{\partial x \partial y}$.[12] Our approach of eq 6 could then be applied to determine surface tension from the variations in $\Delta P - \Delta P_o$ and summed curvature across the analysis points.

Examples of nonaxisymmetric interfaces are those of droplets or bubbles at noncircular orifices; inside of porous media or irregularly shaped cavities; on inclined surfaces; or spanning between wires.[13−17] The geometry of such interfaces could be captured with a three-dimensional imaging method such as optical sectioning microscopy, (micro)computed tomography, or magnetic resonance imaging.

*Potential for Dynamic Analysis.* The present approach to $\gamma$ determination from interfacial contour, like previous approaches, is derived from a static analysis and applies to static droplets and bubbles. Characterization of viscous forces and acceleration, if present, could enable dynamic analysis analogous to that for fluid entrance into a tube.[18] However, such dynamic analysis would be complex for the geometry of a droplet or bubble and even more so in the presence of surfactant. Given this complexity, dynamic conditions are frequently analyzed with a quasi-static approach, in which static analysis is applied to images obtained during expansion or contraction. Much has been learned from quasi-static analyses.[7,10,19] The regression method for $\gamma$ determination could likewise be employed in quasi-static analyses.

## CONCLUSIONS

Along small droplet and bubble interfaces with spread DPPC films, we show that the summed curvature, like $\Delta P$, varies linearly with elevation. Consequently, $\gamma$ is constant and can be determined by linear regression. In doing so, we support an intuitive understanding of how gravity deforms fluid−fluid interfaces and present a new method for determining $\gamma$. Accuracy of the regression method is limited by the accuracy with which curvature can be determined from pixelated images. Nonetheless, agreement between the regression method and ADSA is high, and the accuracy of the regression method will be acceptable for many applications. Finally, the regression method has the potential to be extended to nonaxisymmetric interfaces.

## AUTHOR INFORMATION


### Corresponding Author

**Carrie E. Perlman** − *Department of Biomedical Engineering, Stevens Institute of Technology, Hoboken, New Jersey 07030, United States;* orcid.org/0000-0002-5435-191X; Email: cperlman@stevens.edu

### Authors

**Bret A. Brandner** − *Pulmonary and Critical Care Medicine, Oregon Health & Science University, Portland, Oregon 97239, United States*

**Stephen B. Hall** − *Pulmonary and Critical Care Medicine, Oregon Health & Science University, Portland, Oregon 97239, United States;* orcid.org/0000-0001-8870-2143

Complete contact information is available at: https://pubs.acs.org/10.1021/acs.langmuir.5c02838



### Funding

Supported by grants R01/R56 HL113577 (CEP) and R01 HL136734 (SBH).


### Notes

The authors declare no competing financial interest.

## REFERENCES


(1) Lautrup, B. Chapter 5. Surface Tension. In *Physics of Continuous Matter: Exotic and Everyday Phenomena in the Macroscopic World*; CRC Press, Taylor & Francis Group: Boca Raton, FL, 2011; pp 69−94.

(2) Malcolm, J.; Elliott, C. Interfacial Tension from Height and Diameter of a Single Sessile Drop or Captive Bubble. *Can. J. Civ. Eng.* **1980**, *58*, 151−153.

(3) Saad, S. M. I.; Neumann, A. W. Axisymmetric Drop Shape Analysis (ADSA): An Outline. *Adv. Colloid Interface Sci.* **2016**, *238*, 62−87.

(4) Rachmawan. Canny Edge Detection, v. 1.0.0.0, 2014, (accessed April 1, 2024). https://www.mathworks.com/matlabcentral/fileexchange/46859-canny-edge-detection.

(5) Schoel, W. M.; Schürch, S.; Goerke, J. The Captive Bubble Method for the Evaluation of Pulmonary Surfactant: Surface Tension, Area, and Volume Calculations. *Biochim. Biophys. Acta* **1994**, *1200* (3), 281−290.

(6) Khoojinian, H.; Goodarzi, J. P.; Hall, S. B. Optical Factors in the Rapid Analysis of Captive Bubbles. *Langmuir* **2012**, *28* (39), 14081−14089.

(7) Zuo, Y. Y. Comparative Biophysical Study of Clinical Surfactants Using Constrained Drop Surfactometry. *Am. J. Physiol.: Lung Cell. Mol. Physiol.* **2024**, *327* (4), L535−L546.

(8) Crane, J. M.; Putz, G.; Hall, S. B. Persistence of Phase Coexistence in Disaturated Phosphatidylcholine Monolayers at High Surface Pressures. *Biophys. J.* **1999**, *77* (6), 3134−3143.

(9) Khoojinian, H.; Goodarzi, J. P.; Hall, S. B. Aligning Pitch for Measurements of the Shape of Captive Bubbles. *Colloids Surf. A Physicochem. Eng. Asp.* **2012**, *397*, 59−62.

(10) Schramm, L. L.; Fisher, D. B.; Schurch, S.; Cameron, A. A Captive Drop Instrument for Surface or Interfacial Tension Measurements at Elevated Temperatures and Pressures. *Colloids Surf. A Physicochem. Eng. Asp.* **1995**, *94* (2), 145−159.

(11) Smith, E. C.; Crane, J. M.; Laderas, T. G.; Hall, S. B. Metastability of a Supercompressed Fluid Monolayer. *Biophys. J.* **2003**, *85* (5), 3048−3057.

(12) Patrikalakis, N. M.; Maekawa, T. Chapter 3. Differential Geometry of Surfaces. In *Shape Interrogation for Computer Aided Design and Manufacturing*; Springer: Heidelberg, 2010; pp 49−72.

(13) Cihan, A.; Corapcioglu, M. Y. Effect of Compressibility on the Rise Velocity of an Air Bubble in Porous Media. *Water Res.* **2008**, *44* (4), W04409.

(14) Perazzo, A.; Tomaiuolo, G.; Preziosi, V.; Guido, S. Emulsions in Porous Media: From Single Droplet Behavior to Applications for Oil Recovery. *Adv. Colloid Interface Sci.* **2018**, *256*, 305−325.

(15) Kim, Y.; Gonçalves, M.; Kim, D.-H.; Weon, B. M. Topological Heterogeneity and Evaporation Dynamics of Irregular Water Droplets. *Sci. Rep.* **2021**, *11* (1), 18700.
(16) Wang, C.; Mehmani, Y.; Xu, K. Capillary Equilibrium of Bubbles in Porous Media. *Proc. Natl. Acad. Sci. U.S.A.* **2021**, *118* (17), No. e2024069118.
(17) Zhou, Y.; Ji, B.; Yan, X.; Jin, P.; Li, J.; Miljkovic, N. Asymmetric Bubble Formation at Rectangular Orifices. *Langmuir* **2021**, *37* (14), 4302−4307.
(18) Hamraoui, A.; Nylander, T. Analytical Approach for the Lucas-Washburn Equation. *J. Colloid Interface Sci.* **2002**, *250* (2), 415−421.
(19) Putz, G.; Goerke, J.; Clements, J. A. Surface Activity of Rabbit Pulmonary Surfactant Subfractions at Different Concentrations in a Captive Bubble. *J. Appl. Physiol.* **1994**, *77* (2), 597−605.





https://doi.org/10.1021/acs.langmuir.5c02838
*Langmuir* 2025, 41, 23096−23108